Molecular dynamics simulation of liquid argon flow in a nanoscale channel

Qiangqiang Sun[a], Yong Zhao[b], Kwing-So Choi[a], Xuerui Mao[a,*]

[a] *Faculty of Engineering, University of Nottingham, Nottingham, NG7 2RD, UK.*
[b] *AVIC Aerospace Systems, Chaoyang District, Beijing, 100028, China.*

Abstract

The convective heat transfer in the Micro/ Nanoscale channel is of significant importance in engineering applications, and the classical macroscopic theory is invalid at depicting its physical processes and mechanisms. In this study, molecular dynamics (MD) simulations are conducted to investigate the heat transfer of liquid argon flow through a nanoscale channel. The results show that the fully developed bulk temperature agrees with the continuum based solution of the analytical energy equation at channel height 24 nm, while this agreement reduces with the decrease of the height due to the nanoscale features. At height 6 nm, velocity slip exists around the hydrophobic wall, and enhanced near-wall viscosity of liquid and reduced velocity slip length are observed at larger fluid-wall interaction strength. A region around 2 Å wide without liquid atoms is formed at the hydrophilic wall, leading to a zero velocity in this hollow domain and a no-slip boundary condition. Most importantly, the thermal slip length is remarkably dependent on the liquid density layering in the proximity of the wall and inversely proportional to the first peak value of liquid adjacent to the interface. This observation provides a new idea to tune the heat dissipation properties at the fluid-wall interface by controlling the liquid density layering.

Keywords:
Molecular dynamics simulation, Slip flow, Density layering, Convective heat transfer

1. Introduction

The forced convective heat transfer in hydrodynamically developed and thermally developing laminar flow is also named as the Graetz problem, existing widely in macroscale heat exchangers and nanoscale devices. For example, the miniaturization and the ultra-high processing speed of chips can cause a very high-heat flux, and the temperature of the hotspots resulted from such high heat flux is dramatically higher than the average temperature of the chip [1]. These hotspots pose a thermal bottleneck for the overall reliability of chips, which increases the demand for cooling by using fluid or gas flow through channels [2]. Moreover, nanofluids generated by mixing very small solid particles with the base liquid show fascinating features such as high thermal conductivities and high stability, and have great potential as the heat transfer enhanced fluids can be employed in novel biomedicine and electronic applications [3]. Also, nanopore membranes and nanotube attracting many researchers' attention have high water permeability and solute exclusion, and can be used to reduce the size of the desalination system and improve the energy efficiency by imposing a small temperature difference [4].

The heat transfer in these applications has been systematically investigated based on the continuity hypothesis from the view of energy conservation with no-slip condition on the solid surface for velocity and temperature in the macroscale realm [5]. At Micro/ Nanoscale, however, the forced laminar convective heat transfer shows considerably different physical mechanisms with the macroscale one [6]. For example, a series of investigations [7, 8] demonstrated that the no-slip velocity wall boundary condition commonly applied in macro-level simulations becomes less valid at microscale and nanoscale where wall surface structures dominate the flow and heat transfer behaviors. Similarly, the temperature discontinuity or thermal slip phenomenon at the fluid-wall interface can yield noticeably deviated physical behaviors from that at the macro-level [9]. Besides, a series of distinct molecular layers form the density layering in the vicinity of the fluid-wall interface and

*Corresponding author
Email address: maoxuerui@sina.com (Xuerui Mao)

Nomenclature:

A	constant parameter
A_n	summation coefficients
a_n	coefficients in confluent hypergeometric function
B	constant parameter
Br	Brinkman number
b_n	coefficients in confluent hypergeometric function
c_p	specific heat at constant pressure
D_1, D_2, D_3	domains
D_H	hydraulic diameter ($D_H = 4H$)
d	shortest distant between an atom and its neighbour
fx	body force
Gz	Graetz number
H	half height of the channel
k	thermal conductivity
K_s	spring constant
L	channel length
L_v	velocity slip length
L_T	thermal slip length
L_{T0}	reference value of the thermal slip length
N	number of atoms
Pe	Péclet number
Pr	Prandtl number
Re	Reynolds number
r	distance between two arbitrary particles
r_c	cut off distance in LJ potential
T	temperature
u	velocity component
U	potential energy
V	volume of the channel
W	channel width
x, y, z	cartesian coordinate
z_n	variable in confluent hypergeometric function

Greek symbols

α	thermal diffusivity
β_n	eigenvalues
δ_1, δ_2	height of the small region
$\langle \delta u^2 \rangle$	mean squared displacement about lattice site
ϵ	energy character parameter
η	dimensionless coordinate
μ	dynamic viscosity
ν	kinematic viscosity
ρ	density
σ	collision diameter
θ	non-dimensional temperature
ξ	dimensionless coordinate

Subscripts

Ar	argon
Ag	silver
ave	average value
a	analytical solution
b	bulk value/region
C	critical value
f	fluid properties
fb	first bin
i	inlet properties
l	density layering
m	mean value
p	peak value
w	wall properties

Superscript

$*$	dimensionless quantity

produce the non-uniform density [10] and viscosity [11] profiles.

It should be pointed out that although tremendous effort [12] has been devoted to investigating the Graetz problem using the continuum-based energy equations with velocity and thermal slip wall boundary conditions, the applied slip model contains constant momentum and thermal accommodation coefficients, which, unfortunately, strongly depend on materials of fluids and the wall, local pressure, velocity and the mean direction of the local flow [13]. Consequently, all these factors may lead to the breakdown of the continuum-based model in depicting the Graetz problem at Micro/ Nanoscale. The molecular dynamics (MD) simulation has become an effective alternation to study the nanoscale fluid and heat transfer characteristics as it does not introduce any postulation except the potential functions describing the interforce of particles, and it has been used successfully to calculate the transport parameters (i.e., thermal conductivity) [14, 15]. However, MD studies of the forced convective behaviors and the underlying mechanisms of nanochannel flow are merely explored.

In this work, fluid and heat transfer in a nanoscale channel is investigated by both MD simulations and the analytical solution of the continuum-based energy equation where the accuracy has been fully validated [12]. Results from the two approaches are compared to evaluate the validity of the continuity assumption and to reveal the physical characteristics of molecular-level forced convective heat transfer. Technical details pertaining to MD simulations are illustrated in Section 2, and the results and discussions are presented in Section 3 and Section 4. Finally, conclusions are drawn in Section 5.

2. Methodology of molecular dynamics simulations

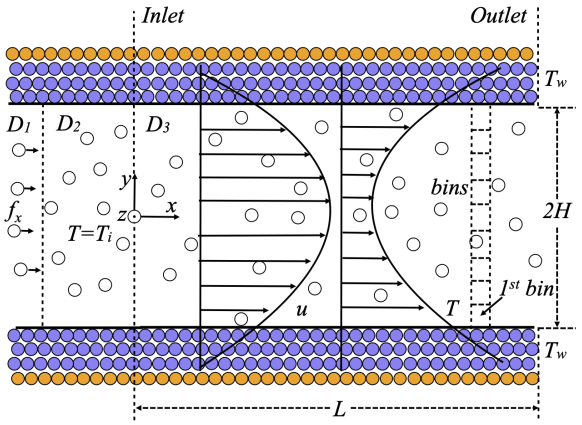

Figure 1: Sketch of the MD simulation system. The modelling domain includes three sub-domains: forcing region D_1, thermostat region D_2 and sample region D_3. Open circles denote liquid argon atoms. The outermost wall atoms (brown circles) are frozen to their initial positions, and the other wall atoms (blue circles) are constrained to corresponding initial locations via virtual springs.

2.1. Governing equations

As shown in Fig. 1, the liquid argon atoms are delivered along the x direction in a parallel plate channel composed of solid silver atoms with the face-centered structure (FCC) and lattice constant 4 Å. Periodic boundary conditions are applied in x and z directions. The motions of particles are governed by

$$\boldsymbol{f}_{ij} = -\nabla U(r_{ij}), \tag{1a}$$

$$m\ddot{\boldsymbol{r}}_i = \boldsymbol{f}_i = \sum_{j=1, j\neq i}^{N_m} \boldsymbol{f}_{ij}, \tag{1b}$$

where $U(r_{ij})$ is the potential energy function, r_{ij} is the magnitude of the distance between two arbitrary particles, $\boldsymbol{f}_{ij}$ is the force that atom j exerts on atom i, m is the atomic mass, $\boldsymbol{r}_i$ is the position of the particle i, $\boldsymbol{f}_i$ is the total force and N_m is the total number of particles in the simulation system. Herein, the 12-6 Lennard-Jones (LJ) pair-wise potential in previous works [16, 17] is used to model the interaction forces for argon-argon, silver-silver and argon-silver atoms

$$U(r_{ij}) = 4\epsilon\left[\left(\frac{\sigma}{r_{ij}}\right)^{12} - \left(\frac{\sigma}{r_{ij}}\right)^{6}\right], \tag{2}$$

where ϵ is the well-depth of the Lennard-Jones potential and σ is the collision diameter. For argon and silver atoms, there are $\epsilon_{Ar-Ar} = 0.0104\,ev$, $\sigma_{Ar-Ar} = 3.405$Å, $\epsilon_{Ag-Ag} = 0.4080\,ev$ and $\sigma_{Ag-Ag} = 2.551$Å, respectively [18]. ϵ_{Ar-Ag} and σ_{Ar-Ag} can be obtained from the Lorenz-Bertholot rule [19, 20]

$$\varepsilon_{Ar-Ag} = \sqrt{\varepsilon_{Ar-Ar}\,\varepsilon_{Ag-Ag}} = 0.0651\,ev, \tag{3a}$$

$$\sigma_{Ar-Ag} = \frac{\sigma_{Ar-Ar} + \sigma_{Ag-Ag}}{2} = 2.978\,\text{Å}. \tag{3b}$$

In the following text, we vary ϵ_{Ar-Ag} with fixed σ_{Ar-Ag} to tune the wetting ability of the wall. For brevity, dimensionless ϵ^*_{Ar-Ag} defined as $\epsilon_{Ar-Ag}/\epsilon_{Ar-Ar}$ is applied. To reduce the computational cost, the Lennard-Jones potential is truncated using a typical cut-off distance $r_c = 2.5\sigma$ [21]. Interactions of two arbitrary atoms are not considered if the distance between them is greater than this cut-off value. Throughout this work, atoms' velocities are updated via the verlet algorithm and $1\,fs$ is chosen as the time step. The first $0.5\,ns$ is used to reach an equilibration phase in the NVT ensemble [22] to thermally relax the MD system before applying artificial forces to drive liquid atoms flow and performing Langevin thermostat. The following $2.5\,ns$ is for the MD system to achieve the steady state and then another $5\,ns$ to collect data.

To drive liquid argon atoms to flow in the x direction, Markvoort et al. [23] artificially added a force f_x for each atom in the D_2 region after resetting the temperature T of atoms in domain D_1 to T_i to meet the inlet temperature boundary condition. However, this force may increase energies of atoms to drive their real temperatures to deviate from desired values, since the externally forced region is located upstream of the thermostat domain. Hence, the order of forcing and thermostat domains is changed herein. Every atom in D_1 moves in x direction driven by the external force f_x. Then, an average velocity u_a is subtracted from each atom's x velocity component before using the Langevin thermostat algorithm [24] to control the temperature in D_2.

2.2. Definition of physical quantities

The local dimensionless temperature of argon atoms is defined as

$$\theta_m(\xi) = \frac{T_m(\xi) - T_w}{T_i - T_w} \text{ with } T_m(\xi) = \frac{\int_0^1 c\rho u(\eta) T(\xi,\eta)\mathrm{d}\eta}{\int_0^1 c\rho u(\eta)\mathrm{d}\eta}, \tag{4}$$

where T_w and T_i are wall temperature and inlet temperature of liquid argon, respectively. ξ and η are dimensionless coordinates in streamwise and spanwise directions,

respectively, defined as $\xi = x/(Pe \cdot H)$ and $\eta = y/H$. H is the half height of the channel.

As aforementioned, there can be velocity and temperature slip on the surface of the wall at the nanoscale. The velocity slip length (L_v) is related with the fluid behaviour including the slip flow magnitude and the potential effects of surface advection, and is given by

$$L_v = \frac{\Delta u_{wf}}{\left.\frac{\partial u}{\partial y}\right|_{y=H}}, \tag{5}$$

where Δu_{wf} is the difference between the wall velocity and the fluid velocity at the wall, and $\left.\frac{\partial u}{\partial y}\right|_{y=H}$ is the velocity gradient of fluid at the interface.

The thermal slip length (L_T) reveals the importance of discontinuity of fluids temperature at the wall, and can be written as

$$L_T = \frac{\Delta T_{wf}}{\left.\frac{\partial T}{\partial y}\right|_{y=H}}. \tag{6}$$

Similarly, ΔT_{wf} is the discrepancy between wall temperature and fluid temperature at the interface, and $\left.\frac{\partial T}{\partial y}\right|_{y=H}$ is the temperature gradient of argon at the wall.

Moreover, the local dynamic viscosity of liquid atoms can be evaluated from [11]

$$\mu = \frac{\tau_{xy}}{\dot{\gamma}}, \tag{7}$$

where τ_{xy} is the shear stress vector, and $\dot{\gamma}$ is the shear rate. For the planar Poiseuille flow, $\dot{\gamma} = \mathrm{d}u(x)/\mathrm{d}y$, and τ_{xy} is determined by the method of planes [25].

2.3. Details of geometrical models

Table 1: Physical parameters for liquid argon at 100K.

Thermal conductivity $[w/(m \cdot K)]$	Dynamic viscosity $(Pa \cdot s)$	Specific heat $[J/(Kg \cdot K)]$
101.24×10^{-3} [26]	0.2×10^{-3} [27]	1.165×10^{3} [28]
110.00×10^{-3} [29]	$(0.18 \pm 0.027) \times 10^{-3}$ [27, 30]	1.156×10^{3} [31]
102.70×10^{-3} [32]	0.194×10^{-3} [33]	

The length of the channel is determined by the inverse Graetz number $\frac{1}{Gz} = \frac{L}{D_H Pe} = 0.4$ in order to ensure that the hydrodynamically developed laminar flow is achieved in the channel [34, 35]. Further, considering the numerical terms introduced in D_1 and D_2 and the periodic boundary condition used in the streamwise direction which induces nonphysical phenomena around the outlet part of D_3, these three sections will be discarded when collecting data samples, as similarly performed in references [9, 35, 36]. Consequently, a larger inverse Graetz number which is proportional to the channel length is chosen

$$\frac{1}{Gz} = \frac{L}{D_H Pe} \approx 1, \tag{8}$$

where Pe is the Péclet number and $Pe = RePr = \rho c_p/\kappa$.

Another key input is the dimensionless density (ρ^*). We choose $\rho^* \approx 0.8$ and the initial temperature T_0 is set to $100K$ which corresponds to the liquid state of argon [33, 37]. The geometrical dimensions of the channel and the number of argon atoms inside the channel should satisfy the following equation

$$\rho^* = \frac{N}{V}\sigma_{Ar-Ar}^3 = \frac{N}{LWH}\sigma_{Ar-Ar}^3 \approx 0.8. \tag{9}$$

Moreover, Haji-Sheikh et al. [38] and Haddout et al. [39] stressed that the axial conduction (see Eq. (A.2)) influence needs to be considered when the Péclet number (Pe) is less than 10 after applying the series analysis solution approach to study the temperature distributions in parallel plate channels or circular ducts, respectively. Further, Hennecke [40] stated that axial conduction might be neglected at $Pe > 20$. To fully clarify the limitation of analytical models in various situations, Pe within the following three intervals was tested in this work: $Pe_1 \in (0, 10)$, $Pe_2 \in (10, 20)$ and $Pe_3 \in (20, +\infty)$.

Similar to reference [41], physical parameters for the liquid argon are postulated as constant as shown in Table 1. Considering Eqs. (8) and (9), and the geometrical dimensions of the channel, the total number of fluid atoms and average velocities are selected (shown in Appendix B for clarity).

In the entire simulation process, the outmost silver atoms are frozen to their respective FCC lattice sites to prevent losing wall atoms, and the remaining silver atoms are constrained to their initial lattice sites via using the virtual harmonic spring. This mimics wall atoms' real motions as it allows these particles to oscillate [42]. The following factors should be considered when choosing the value of the spring constant: (1) maintaining well-defined wall boundary structures with a computationally acceptable number of particles; (2) ensuring that the distance between wall atoms is small enough to prevent fluid particles leaking through the wall [43]; (3) preventing solid wall particles from being over-constrained during the process of molecular dynamics simulations [42]. Based on these constraints, Thompson et al. [44] argued that this parameter

can be evaluated according to the Lindemann criterion: $\left\langle \delta u^2 \right\rangle / d^2 < 0.023$. $\left\langle \delta u^2 \right\rangle$ is the mean squared displacement about the lattice site and d is the nearest-neighbour distance. However, it is complex to determine the spring constant through the Lindemann criterion as some parameters in this rule have to be obtained from neutron scattering experiments. Khare R et al. [45] proposed another straightforward method to estimate the spring constant

$$K_s = \frac{500\varepsilon}{\sigma^2}. \tag{10}$$

Based on this criteria, the spring constant is $502\, N/m$ as will be used throughout this work.

2.4. Validation

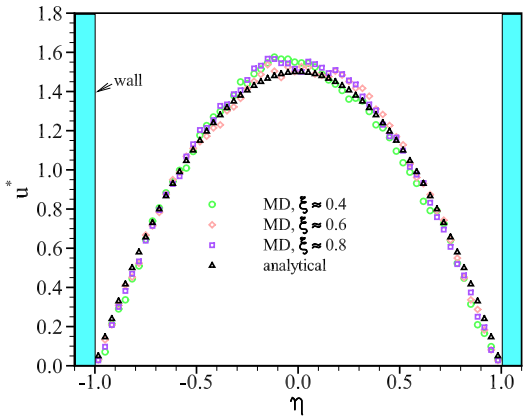

Figure 2: Velocity profiles at $T_w = 190\, K$ and $H = 12\, nm$. For the analytical result, $u^* = u/u_a = 3/2(1-\eta^2)$.

The variation of streamwise velocity u on three cross sections ($\xi = 0.4$, 0.6 and 0.8) obtained from MD simulations is illustrated in Fig. 2. The parabolic velocity profile predicted by the analytical solution is duplicated by the MD simulation in all the three cross-sections. Hence, flow in the plane parallel channel driven by the approach introduced in Section 2.1 can be treated as hydrodynamically developed laminar flow [9, 23, 35, 36]. Moreover, one interesting observation is that there is no velocity slip (similarly, no velocity slip is observed for $H = 3$ or $6\, nm$, and the corresponding velocity profiles are not reported here for brevity). It will be illustrated later that this is owing to the large value of energy parameter (ϵ_{Ar-Ag}) calculated from the Lorenz-Bertholot rule.

Also, two cross-sections are chosen and the corresponding temperature profiles along the channel height

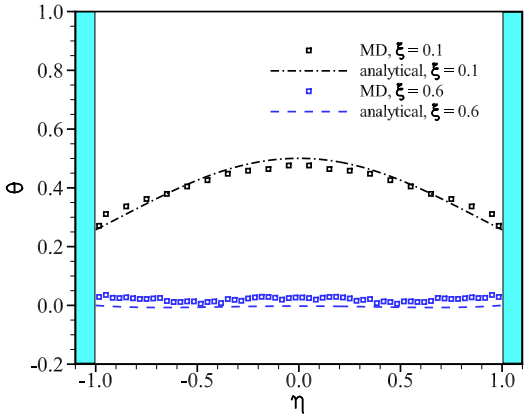

Figure 3: Dimensionless temperature profile at mean velocity $u_a \approx 33.5\, m/s$, $\epsilon^*_{Ar-Ag} = 6.26$, $H = 12\, nm$ and $T_w = 190\, K$.

direction are shown in Fig. 3. One can see that the temperature calculated from the MD simulation and analytical solution coincide with each other.

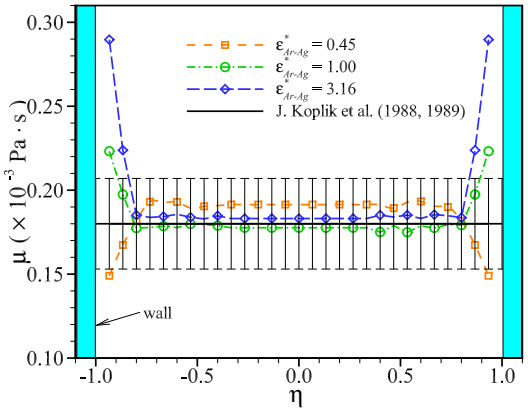

Figure 4: Effects of wall wettability on the dynamic viscosity of the liquid argon at $H = 6\, nm$, $T_w = 150\, K$ and $u_a \approx 33.5\, m/s$.

In addition, the local viscosity profiles are also calculated. As shown in Fig. 4, the bulk viscosity shows good agreement with experiment data marked by the black line (the relative error is less than 5%). However, the viscosity at the wall-fluid interface deviates from the bulk value, and exhibits an upward trend at larger wall-fluid interaction strength. These observations of the velocity, temperature and viscosity validate the correctness of the calculations in this work.

3. Limitation of the continuum-based analytical model in predicting temperature

As aforementioned in Section 1, the continuum-based energy equation (see Appendix A) becomes less valid when depicting nanoscale flow and heat transfer problems due to the violation of the no-slip boundary conditions, the non-uniform density profile, etc. The convective heat transfer in the nanoscale channel shown in Fig. 1 is explored by both the MD simulation and the energy equation.

3.1. Effects of viscous dissipation and axial conduction on the temperature profile

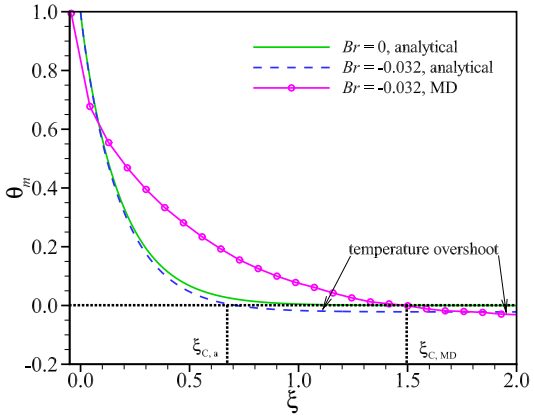

Figure 5: Effects of the viscous dissipation on the bulk mean temperature distributions at $Pe = 6.218$.

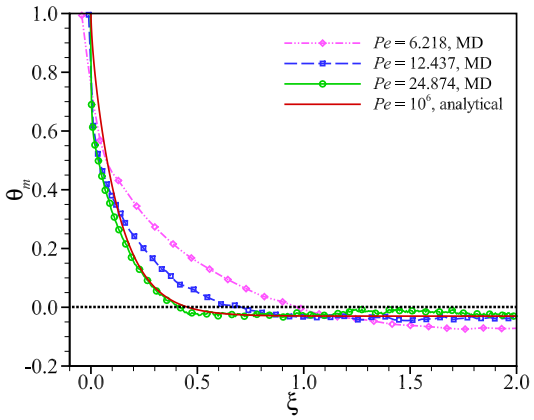

Figure 6: Effects of the axial conduction on the bulk mean temperature distributions at $Br = -0.044$.

Fig. 5 shows the effect of the viscous dissipation on the dimensionless bulk temperature of liquid argon. Based on the analytical solution of the 2D energy equation, the effect of the viscous dissipation term shown in Eq. (A.2) on heat transfer can be eliminated by setting $Br = 0$. Then, one can find that the fully developed bulk mean temperature is 0 (namely, fluid and wall temperature are equal to each other). However, there is a critical point $\xi_{C,a}$ where the bulk temperature $\theta_m = 0$ as reported in a previous study [12]. The fluid temperature will exceed wall temperature (we term this phenomenon as "temperature overshooting") after this critical point when considering the viscous dissipation. Although analytical solutions mentioned above tend to underestimate the critical point, the temperature overshooting is also observed in the MD simulations. This validates the correctness of analytical solutions of the energy equation and the important role of viscous dissipation in heat transfer of microscale channels.

The bulk temperature neglecting axial conduction effects is obtained from the analytical solution by setting $Pe = 10^6$, similar to references [12, 41]. Three cases including $Pe = 6.218$, $Pe = 12.437$ and $Pe = 24.874$ are simulated by the MD method. As shown in Fig. 6, the impacts of axial conduction on fully developed or local bulk mean temperature of the fluid can be eliminated at $Pe \gtrsim 12.437$ or $Pe \gtrsim 24.874$, respectively.

The bulk non-dimensional temperature (θ_m) of liquid argon is shown in Fig. 7. Clearly, a higher energy parameter leads to lower dimensionless temperature over the thermally undeveloped region, but this effect vanishes when reaching the fully developed region. The analytical solution obtained by assuming the fluid dynamics is continuous and the density is constant (see Appendix A) is also plotted. This analytical solution predicts well the temperature at high enough energy parameter but at low values of ξ, it underestimates the dimensionless temperature. When the channel becomes smaller, the discrepancy between the analytical and MD solutions also increases as the continuity assumption becomes less valid. These two parameters, ξ and H, will be further explored in the following section.

4. Results of MD simulations

The density oscillation, slip boundary conditions and viscosity variation are not accounted in the continuum based analytical model and are the significant features of the Micro/ Nanoscale flow. Hence, the underlying physical mechanisms of the non-uniform density, slip, viscosity variation and their influences on the velocity and temperature profiles are examined by MD simulations in this section.

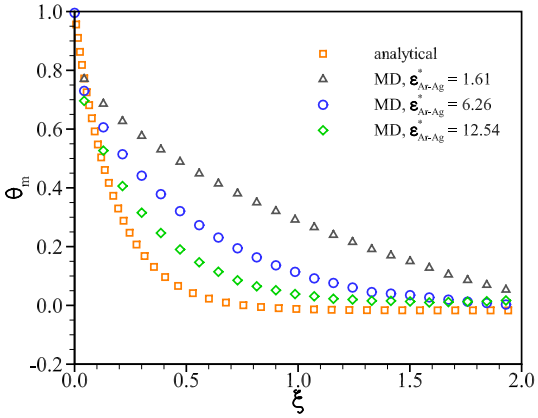

(a) $H = 3\,nm$

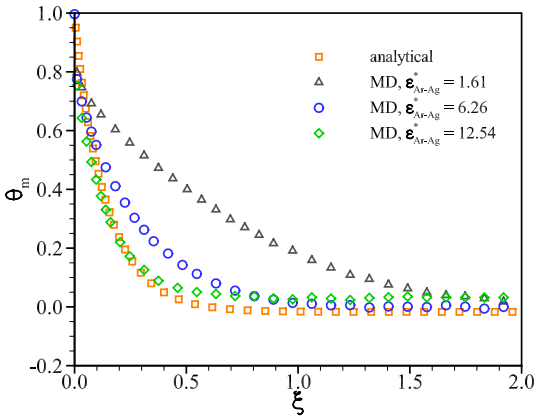

(b) $H = 6\,nm$

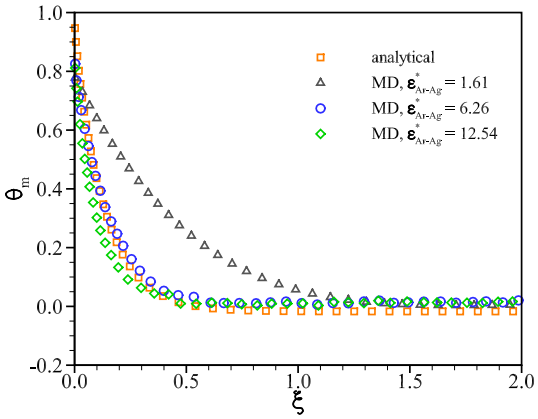

(c) $H = 12\,nm$

Figure 7: Dimensionless bulk temperature profile at mean velocity $u_a \approx 33.5\,m/s$ and $T_w = 190\,K$.

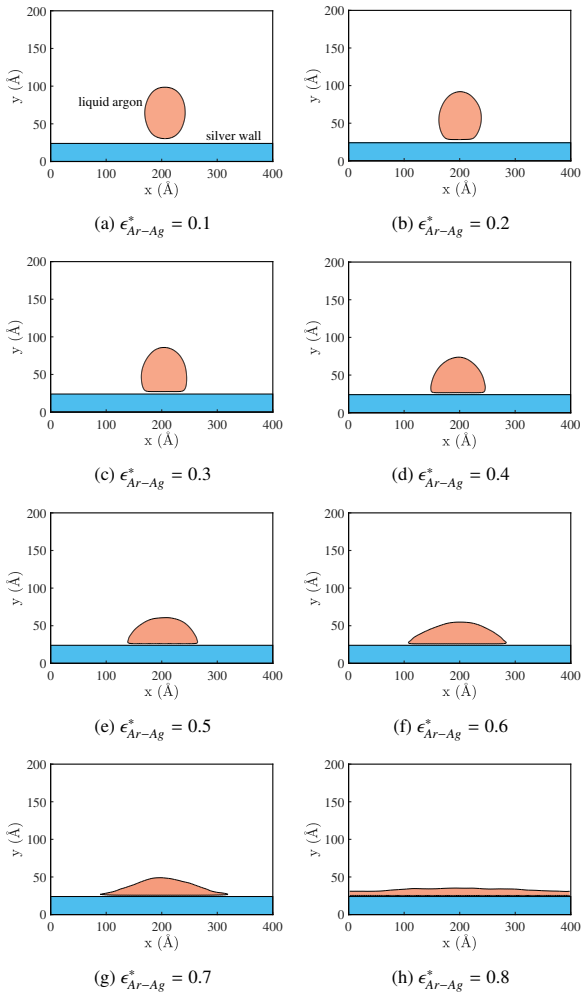

(a) $\epsilon^*_{Ar-Ag} = 0.1$ (b) $\epsilon^*_{Ar-Ag} = 0.2$

(c) $\epsilon^*_{Ar-Ag} = 0.3$ (d) $\epsilon^*_{Ar-Ag} = 0.4$

(e) $\epsilon^*_{Ar-Ag} = 0.5$ (f) $\epsilon^*_{Ar-Ag} = 0.6$

(g) $\epsilon^*_{Ar-Ag} = 0.7$ (h) $\epsilon^*_{Ar-Ag} = 0.8$

Figure 8: Snapshots of the liquid argon droplet at various ϵ^*_{Ar-Ag}.

4.1. *Effects of the well-depth of the LJ potential function on the wall wettability*

As clarified in a previous study [46], the wall wettability can be adjusted by varying the energy parameter of the LJ potential describing the interactions between liquid argon atoms and the wall. Herein, we show the contact angle of the liquid argon droplet on the silver wall by performing MD simulations, and the snapshots of the droplet can be seen in Fig. 8. One can observe that the wall changes from the hydrophobic to hydrophilic one at larger ϵ^*_{Ar-Ag}. Therefore, in the following text, the effects of the wall wettability on the Micro/ Nanoscale flow features mentioned above are investigated by varying ϵ^*_{Ar-Ag} with fixed σ_{Ar-Ag} to tune the wall wettability. Besides, the contact angles at various ϵ^*_{Ar-Ag} are measured, as shown in Fig. 9. Clearly, the cosine of the contact angle is almost a linear function of ϵ^*_{Ar-Ag} over the parameters studied.

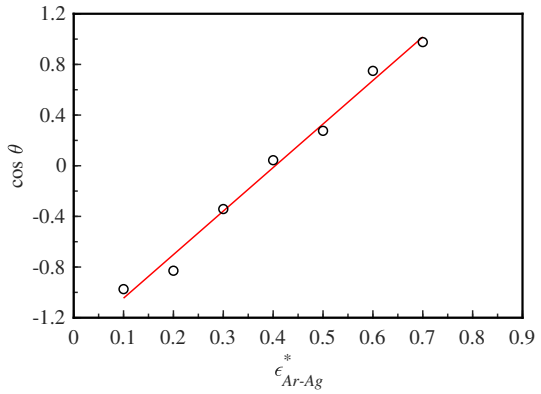

Figure 9: Effects of ϵ^*_{Ar-Ag} on the contact angle. Curves and scatter points are computed from fitting and simulation results, respectively.

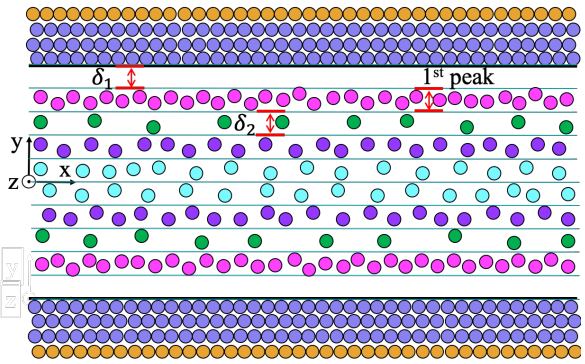

Figure 10: Density profile at mean velocity $u_a \approx 33.5\,m/s$, $T_w = 150\,K$, $H = 3\,nm$ and $\epsilon^*_{Ar-Ag} = 6.26$. Blue and brown circles represent wall atoms, and the other circles denote liquid argon atoms.

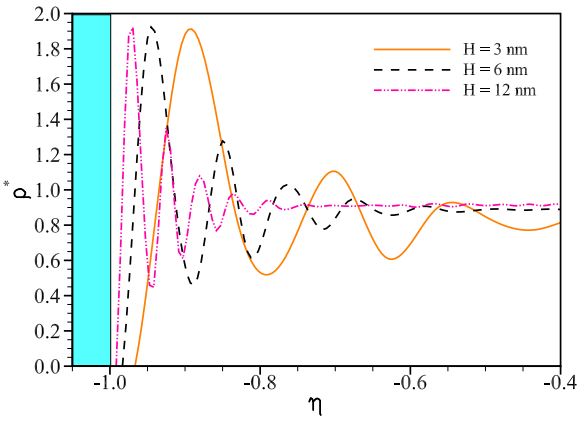

(a)

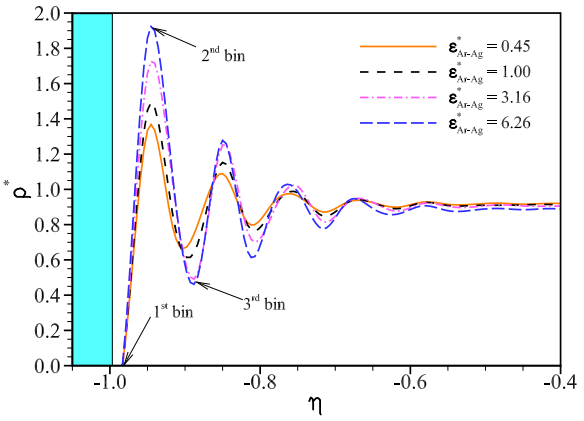

(b)

Figure 11: Dimensionless density ρ^* profile at the cross section with $\xi = 0.13$ for varying (a) channel height H ($u_a \approx 33.5\,m/s$, $\epsilon^*_{Ar-Ag} = 6.26$, and $T_w = 150\,K$) and (b) interaction strength ϵ^*_{Ar-Ag} ($u_a \approx 33.5\,m/s$, $T_w = 150\,K$, and $H = 6\,nm$).

4.2. *Density profile*

Fig. 10 schematically shows the density distribution obtained from MD simulations. Similar to reference [47], a clear stratification in the y direction can be observed and in the literature it has been linked to the oscillatory force curve [48] or the energy scale [49]. There are no liquid argon atoms in an extremely thin layer around 2 Å adjacent to the wall denoted as δ_1 in agreement with a previous observation that the thickness of the hollow layer is is typically less than a nanometer [50]. Then, argon atoms form a high density layer followed by another low density region δ_2. The further inwards layers are less notable and the profile becomes more uniform.

As the channel height results in strong differences between the MD and analytical solutions, its influence on the density profile is studied, as shown in Fig. 11a. Results agree with the expectations that the length of the density fluctuation zone declines for increasing channel heights, confirming that the density fluctuation is only prominent in small scale channel flows. Fig. 11b shows that the dimensional density peak values increase with ϵ^*_{Ar-Ag} [6, 51]. However, the peak location of the density and the length of the density fluctuation region are almost unaffected by the wall wettability. In addition, the wall temperature has no significant effects on the density fluctuation profile over the parameters considered (the corresponding figure is not shown here for brevity).

One interesting observation is that the total number of argon atoms in the density layering region denoted as D_l in Fig. 12 at various ϵ^*_{Ar-Ag} is almost a constant value. The larger magnitude of oscillation at higher ϵ^*_{Ar-Ag} indicates some argon atoms move from the first and other bins to the second bin, as schematically shown

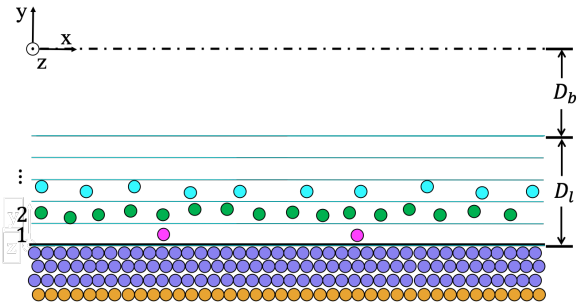

(a) $\epsilon^*_{Ar-Ag} = 0.45$

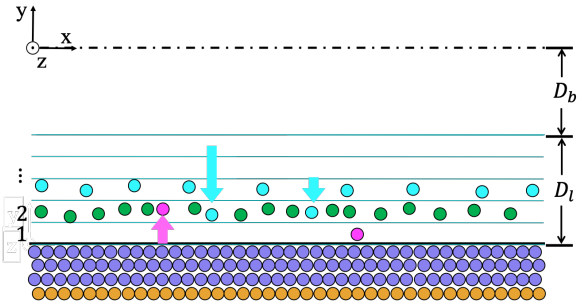

(b) $\epsilon^*_{Ar-Ag} = 1.00$

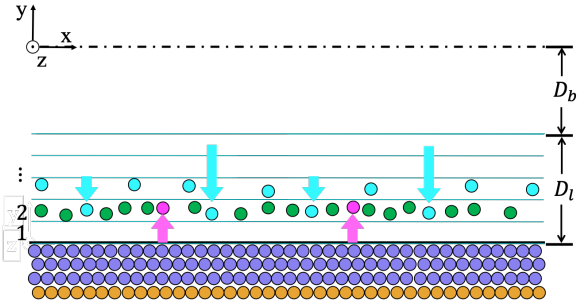

(c) $\epsilon^*_{Ar-Ag} = 3.16$

Figure 12: Density profile in bins in the proximity of the wall at $H = 6\,nm$, $T_w = 150\,K$ and $u_a \approx 33.5\,m/s$. Only the lower part of the model is shown due to symmetry. Blue and brown circles represent wall atoms, and the other circles denote liquid argon atoms. D_b and D_l represent the density bulk and layering regions, respectively.

in Fig. 12.

4.3. Velocity and thermal slip lengths

After clarifying the density layering phenomenon, the hydrodynamic and thermal slip lengths as another two factors causing the violation of the continuum-based model are then investigated based on the MD simulations to illustrate microscopic mechanisms.

Based on simulation results, the velocity slip length over the range of mean velocity studied ($27.2\,m/s \leq u_a \leq 100\,m/s$) is $0.61 \pm 0.046\,nm$, agreeing with that in reference [52]. Similarly, the thermal slip length is also observed to remain relatively constant at $9.34 \pm 1.185\,nm$ at various mean velocity, in agreement with reference [35]. Also, the velocity and temperature slip lengths at various channel height are shown in Fig. 13. Similar to reference [53], the slip length converges to almost a constant value at a larger H.

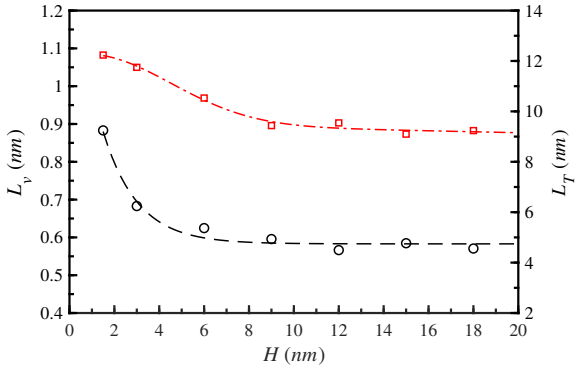

Figure 13: Velocity and temperature slip lengths at $\epsilon^*_{Ar-Ag} = 0.45$, $T_w = 150\,K$ and $u_a \approx 33.5\,m/s$. The red and black curves denote the temperature and velocity slip lengths, respectively.

Then, effects of the non-dimensional energy parameter ϵ^*_{Ar-Ag} in the LJ potential function characterising the wall wettability on the two slip lengths are studied. A significant decrease in velocity slip length from 0.62 to $0\,nm$ is obtained by increasing the dimensionless energy parameter from $\epsilon^*_{Ar-Ag} = 0.45$ to $\epsilon^*_{Ar-Ag} = 1.00$, as can be seen in Fig. 14a. The reduction of L_v can also be observed intuitively from the velocity profile along the channel height direction in Fig. 14b. Meanwhile, one can find that the dimensionless density in the first bin ρ^*_{fb} drops dramatically at larger ϵ^*_{Ar-Ag} and reaches 0 at $\epsilon^*_{Ar-Ag} \geqslant 3.16$. This indicates all liquid argon atoms are ejected from the hole region closest to the hydrophilic wall as schematically plotted in Fig. 12 and therefore no velocity slip phenomenon is observed.

The effect of the liquid density layering on the thermal slip length (L_T) is further investigated as it is closely related to the layering or the density peak of liquid adjacent to the wall [54–56]. We again tune the wall wetting ability and the interfacial density profile of argon by adjusting ϵ_{Ar-Ag} with fixed σ_{Ar-Ag} for the LJ potential energy function. To quantify the difference of liquid argon density at various ϵ^*_{Ar-Ag} , a new variable is defined as

$$\rho^*_p = \frac{\rho_p}{\rho_b}\,, \tag{11}$$

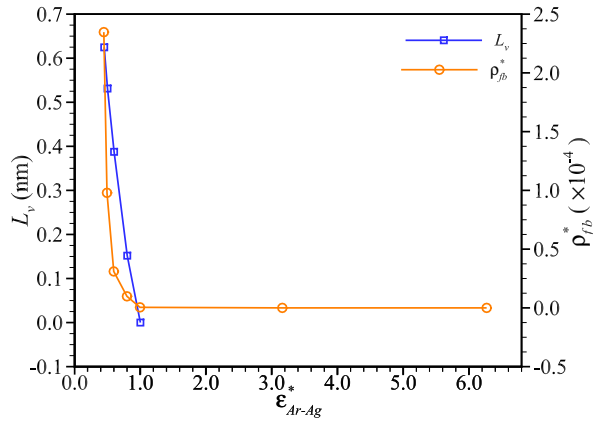

(a) Velocity slip length and density of argon in the first bin.

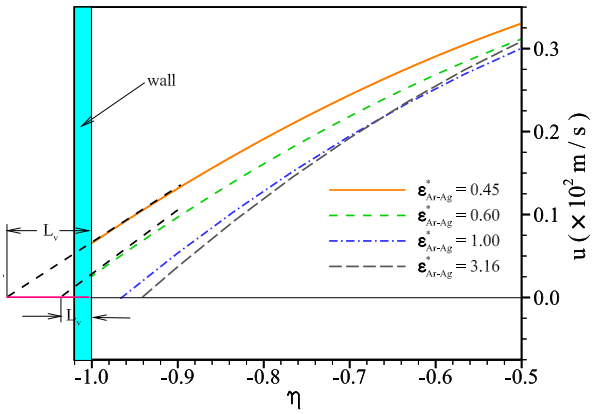

(b) Velocity profiles.

Figure 14: Effects of wall wettability on the velocity slip length and density profile of the first bin at $H = 6\,nm$, $T_w = 150\,K$ and $u_a \approx 33.5\,m/s$.

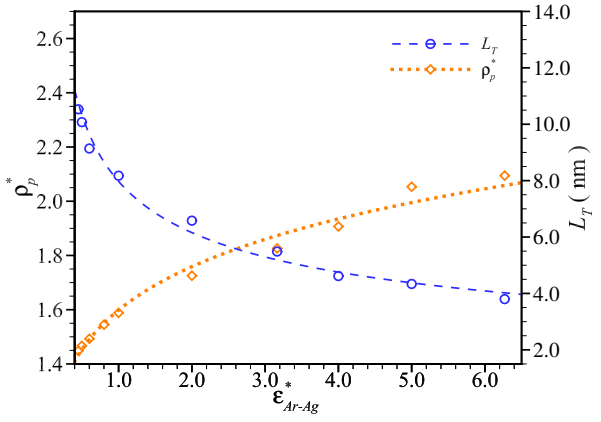

Figure 15: Effects of wall wettability on the temperature slip length and the first density peak of the liquid argon at $H = 6\,nm$, $T_w = 150\,K$ and $u_a \approx 33.5\,m/s$.

where ρ_p is the first peak value of density and ρ_b is the bulk argon density far away from the interface. It is seen in Fig. 15 that L_T varies from 10.53 nm for a hydrophobic wall ($\epsilon^*_{Ar-Ag} = 0.45$) to 3.80 nm for a hydrophilic wall ($\epsilon^*_{Ar-Ag} = 6.26$). This observation aligns with previous reports [57, 58] that the wall wettability has a noticeable effect on L_T. Furthermore, the thermal slip length is found to be correlated with ρ^*_p: the higher the first density peak of liquid argon, the lower the thermal slip length. This coincides with the previous experiment result [59] and molecular simulations [56] where water molecules confined by two graphene layers with different constant temperatures vibrate freely. Also, all of the simulation data are fitted by the following function

$$\frac{L_T}{L_{T0}} = \frac{A}{\rho^*_p + B}, \tag{12}$$

where L_{T0} is the thermal slip length at $\epsilon^*_{Ar-Ag} = 6.26$ calculated from the Lorenz-Bertholot rule in Section 2.1. The correlation factor for the fit is 0.986 and the standard deviations is about 5.74% by setting $A = 1.14$ and $B = -1.04$. However, the mechanism underpinning this correlation is unclear and further study is expected.

5. Conclusions

The liquid argon flow through a nanoscale channel is investigated by MD simulations and analytical modelling. The solution of the MD simulation deviates from the analytical one, which is based on the continuum assumption, as the height of the channel reduces. Then the nanoscale features violating this assumption are examined.

When considering the viscous dissipation that is generally neglected in macroscale heat transfer, the fully developed temperature of the fluid is higher than the constant wall temperature even if the inlet temperature of the fluid is lower than the wall temperature.

The wall material changes from a hydrophobic to hydrophilic one at larger interaction parameters. More specifically, the cosine of the contact angle is almost a linear function of the interaction parameter.

The density profile of argon atoms is found to exhibit a strong oscillation in the proximity of the fluid-wall interface named as the density layering regions, and then converges to the bulk value ($\rho^* \approx 0.8$) in the bulk domain further from the interface. The effect of wall wettability on ρ^* mainly concentrates on the density layering domain and the peak value of ρ^* next to the interface increases at the hydrophilic wall surface. The non-dimensional density layering region widens considerably at smaller channel height.

A dramatic reduction of the velocity slip length is observed when moving from hydrophobic to hydrophilic surfaces. For the super hydrophilic wall, the formation of a thin layer without liquid atoms at the wall-fluid interface weaken and even impede the velocity slip. The thermal slip length is noticeably affected by the liquid argon atoms layering in the proximity of the wall and more specifically by the first peak value of argon atoms adjacent to the fluid-wall interface. Hence, the thermal slip length can be tuned via varying the wall wettability to change the first density peak value. These findings offer a new understanding of velocity and thermal slip at the interface, which can be applied to study the flow and heat dissipation at the nanoscale.

6. Acknowledgements

We gratefully acknowledge the financial support from China Scholarship Council (CSC). This project has received funding from the European Union's Horizon 2020 research and innovation programme under the Marie Skłodowska-Curie grant agreement No 777717.

Appendix A. Analytical solution of the 2D energy equation

Assuming that fluid density, thermal conductivity, specific heat and dynamic viscosity are constant, and defining four non-dimensional quantities as

$$\xi = \frac{x}{Re \cdot Pr \cdot H}, \qquad \eta = \frac{y}{H}, \\ \theta = \frac{T - T_w}{T_i - T_w}, \qquad Br = \frac{\mu u_a^2}{k\,(T_i - T_w)}, \tag{A.1}$$

the dimensionless energy equation including axial conduction and viscous dissipation, and corresponding boundary conditions for the liquid argon flow through a 2D parallel plate channel (see Section 2) can be written as

$$\frac{1}{4} u^* \frac{\partial \theta}{\partial \xi} = \underbrace{\frac{1}{Pe^2} \frac{\partial^2 \theta}{\partial \xi^2}}_{axial\ conduction} + \frac{\partial^2 \theta}{\partial \eta^2} + \underbrace{Br \left(\frac{\partial u^*}{\partial \eta} \right)^2}_{viscous\ dissipation}. \tag{A.2}$$

$$\theta = 1 \qquad at \qquad \xi = 0, \tag{A.3a}$$

$$\frac{\partial \theta}{\partial \eta} = 0 \qquad at \qquad \eta = 0, \tag{A.3b}$$

$$\theta = 0 \qquad at \quad \eta = 1, \tag{A.3c}$$

where the non-dimensionless velocity u^* is

$$u^* = \frac{u}{u_a} = \frac{3}{2}\left(1 - \eta^2\right). \tag{A.4}$$

After utilizing the separation of variables and the variable substitution approach, the infinite series solution of the 2D non-dimensional energy equation can be expressed as

$$\theta = Br\left(\frac{-3}{4}\eta^4 + \frac{3}{4}\right) + \sum_{n=1}^{\infty} A_n \cdot \\ \left[\sum_{m=0}^{\infty} \frac{(a_n)^{(m)} (z_n)^m}{(b_n)^{(m)} m!} exp\left(\frac{-1}{2} z_n\right)\right] exp\left(-\beta_n^2 \xi\right), \tag{A.5}$$

where a_n, b_n as parameters of the confluent hypergeometric function and z_n are

$$a_n = \frac{-\beta_n^3 - \frac{3}{8} Pe^2 \beta_n + \sqrt{\frac{3}{8}} Pe^2}{4\sqrt{\frac{3}{8}} Pe^2}, \\ b_n = \frac{1}{2}, \\ z_n = \sqrt{\frac{3}{8}} \beta_n \eta^2. \tag{A.6}$$

The summation cnstants A_n can be determined from the boundary condition via applying the Gram-Schmidt orthogonal procedure which is illustrated detailedly in appendix of another our work.

The dimensionless bulk temperature of liquid argon is given by

$$\theta_m(\xi) = \int_0^1 u^*(\eta)\, \theta(\xi, \eta)\, d\eta. \tag{A.7}$$

In this appendix, we only outline the process of addressing the 2D energy equation for convective heat transfer in parallel plate flow with non-slip boundary condition. The accuracy validation about the energy equation solution can be found in anther our work [12].

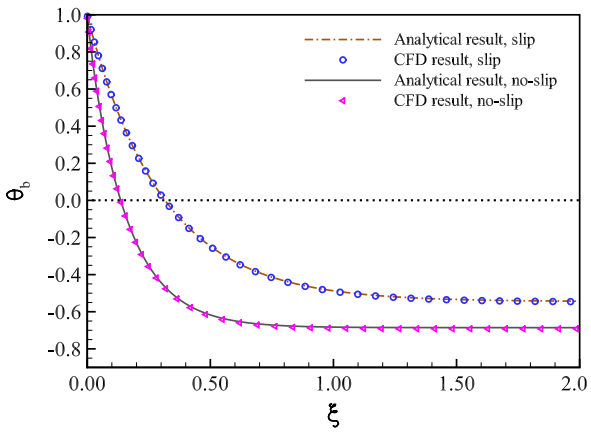

Figure A.16: Dimensionless bulk temperature profile obtained from CFD simulations and analytical solutions at $Pe = 10, Br = -1, Kn = 0.1$.

Besides, the temperature and velocity slip boundary conditions shown in Eq. (A.8) are implemented based on the OpenFOAM (the implementation details can be seen in our previous work [60]). Then, a case is tested by the open-source code and the aforementioned analytical solution, and the outcome is shown in Fig. A.16.

$$\begin{aligned} T - T_w &= L_T \frac{\partial T}{\partial n}, \\ u - u_w &= L_u \frac{\partial u}{\partial n}, \end{aligned} \tag{A.8}$$

where T_w is the wall temperature and u_w is the wall velocity. L_T and L_u are the temperature and velocity slip lengths, respectively. $\partial T/\partial n$ and $\partial u/\partial n$ are the thermal and velocity gradients on the liquid side, respectively.

One can observe that the dimensionless bulk temperature computed from these two methods coincide with other. All comparisons, therefore, indicate that our non-dimensional analytical solution has sufficient accuracy.

Appendix B. Details of geometrical models

Table B.2: Geometrical dimensions of the parallel plate channel and control parameters for $\epsilon_{Ar-Ag} = 0.0651\,ev$ and $\sigma_{Ar-Ag} = 2.978$Å.

u_a (m/s)	$2H$ (nm)	L (nm)	W (nm)	T_w (K)	Pe	N_f	L_{D_1} (nm)	L_{D_2} (nm)
33.50	24	1069.2	3.2	150	24.874	16640211	.2	2
33.50	24	1069.2	3.2	190	24.874	16640211	.2	2
33.50	12	267.2	3.2	150	12.437	207924	1.6	1.6
33.50	12	267.2	3.2	190	12.437	207924	1.6	1.6
33.50	6	66.8	3.2	150	6.218	25990	1.6	1.6
33.50	6	66.8	3.2	190	6.218	25990	1.6	1.6

References

[1] C. Ji, Y. Yan, A molecular dynamics simulation of liquid–vapour–solid system near triple-phase contact line of flow boiling in a microchannel, Applied thermal engineering 28 (2-3) (2008) 195–202.

[2] R. Wu, X. Zhang, Y. Fan, R. Hu, X. Luo, A bi-layer compact thermal model for uniform chip temperature control with non-uniform heat sources by genetic-algorithm optimized microchannel cooling, International Journal of Thermal Sciences 136 (2019) 337–346.

[3] W. Cui, Z. Shen, J. Yang, S. Wu, Effect of chaotic movements of nanoparticles for nanofluid heat transfer augmentation by molecular dynamics simulation, Applied Thermal Engineering 76 (2015) 261–271.

[4] K. Zhao, H. Wu, Fast water thermo-pumping flow across nanotube membranes for desalination, Nano Letters 15 (6) (2015) 3664–3668.

[5] L. Graetz, Uber die warmeleitungsfahighevon von flussingkeiten, part 2, Annalen der Physik und Chemie 25 (1885) 337–357.

[6] M. B. Motlagh, M. Kalteh, Investigating the wall effect on convective heat transfer in a nanochannel by molecular dynamics simulation, International Journal of Thermal Sciences 156 (2020) 106472.

[7] J. A. Thomas, A. J. McGaughey, Reassessing fast water transport through carbon nanotubes, Nano letters 8 (9) (2008) 2788–2793.

[8] A. K. Sadaghiani, A. Koşar, Numerical investigations on the effect of fin shape and surface roughness on hydrothermal characteristics of slip flows in microchannels with pin fins, International Journal of Thermal Sciences 124 (2018) 375–386.

[9] S. Ge, Y. Gu, M. Chen, A molecular dynamics simulation on the convective heat transfer in nanochannels, Molecular Physics 113 (7) (2015) 703–710.

[10] S. Gruener, D. Wallacher, S. Greulich, M. Busch, P. Huber, Hydraulic transport across hydrophilic and hydrophobic nanopores: Flow experiments with water and n-hexane, Physical Review E 93 (1) (2016) 013102.

[11] T. Q. Vo, M. Barisik, B. Kim, Near-surface viscosity effects on capillary rise of water in nanotubes, Physical Review E 92 (5) (2015) 053009.

[12] Q. Sun, K.-S. Choi, X. Mao, An analytical solution of convective heat transfer in microchannel or nanochannel, International Communications in Heat and Mass Transfer 117 (2020) 104766.

[13] G. Karniadakis, A. Beskok, N. Aluru, Microflows and nanoflows: fundamentals and simulation, Vol. 29, Springer Science & Business Media, 2006.

[14] Z. Fan, L. F. C. Pereira, H.-Q. Wang, J.-C. Zheng, D. Donadio, A. Harju, Force and heat current formulas for many-body potentials in molecular dynamics simulations with applications to thermal conductivity calculations, Physical Review B 92 (9) (2015) 094301.

[15] M. Sahebi, A. Azimian, A molecular dynamics study about the mechanisms of liquid thermal transpiration flow in nanotubes, International Journal of Thermal Sciences 136 (2019) 9–14.

[16] N. Wu, L. Zeng, T. Fu, Z. Wang, X. Deng, Mechanism of heat transfer enhancement by nanochannels copper plate interface wettability: A molecular dynamics study, International Journal of Thermal Sciences 159 106589.

[17] L. Zhang, J. Xu, G. Liu, J. Lei, Nucleate boiling on nanostructured surfaces using molecular dynamics simulations, International Journal of Thermal Sciences 152 (2020) 106325.

[18] M. Papanikolaou, Molecular dynamics simulations of confined liquids in nanochannels with rough walls (2017).

[19] H. Lorentz, Ueber die anwendung des satzes vom virial in der kinetischen theorie der gase, Annalen der physik 248 (1) (1881) 127–136.
[20] D. C. R. Berthelot, No title, Hebd. Seanc. Acad. Sci. 126 (1) (1898) 1703.
[21] D. C. Rapaport, D. C. R. Rapaport, The art of molecular dynamics simulation, Cambridge university press, 2004.
[22] W. G. Hoover, Canonical dynamics: equilibrium phase-space distributions, Physical review A 31 (3) (1985) 1695.
[23] A. J. Markvoort, P. Hilbers, S. Nedea, Molecular dynamics study of the influence of wall-gas interactions on heat flow in nanochannels, Physical review E 71 (6) (2005) 066702.
[24] T. Schneider, E. Stoll, Dynamics of the sine-gordon chain, Physical Review Letters 41 (21) (1978) 1429.
[25] B. Todd, D. J. Evans, P. J. Daivis, Pressure tensor for inhomogeneous fluids, Physical Review E 52 (2) (1995) 1627.
[26] B. H. Kim, A. Beskok, T. Cagin, Molecular dynamics simulations of thermal resistance at the liquid-solid interface, The Journal of chemical physics 129 (17) (2008) 174701.
[27] J. Koplik, J. R. Banavar, J. F. Willemsen, Molecular dynamics of fluid flow at solid surfaces, Physics of Fluids A: Fluid Dynamics 1 (5) (1989) 781–794.
[28] C. Gladun, The specific heat of liquid argon, Cryogenics 11 (3) (1971) 205–209.
[29] A. McGaughey, M. Kaviany, Thermal conductivity decomposition and analysis using molecular dynamics simulations. part i. lennard-jones argon, International Journal of Heat and Mass Transfer 47 (8-9) (2004) 1783–1798.
[30] J. Koplik, J. R. Banavar, J. F. Willemsen, Molecular dynamics of poiseuille flow and moving contact lines, Physical review letters 60 (13) (1988) 1282.
[31] O. Rice, The thermodynamic properties of liquid argon, The Journal of Chemical Physics 14 (5) (1946) 324–338.
[32] P. Borgelt, C. Hoheisel, G. Stell, Exact molecular dynamics and kinetic theory results for thermal transport coefficients of the lennard-jones argon fluid in a wide region of states, Physical Review A 42 (2) (1990) 789.
[33] B. H. Kim, A. Beskok, T. Cagin, Viscous heating in nanoscale shear driven liquid flows, Microfluidics and nanofluidics 9 (1) (2010) 31–40.
[34] J. Lahjomri, A. Oubarra, Analytical solution of the graetz problem with axial conduction, Journal of heat transfer 121 (4) (1999) 1078–1083.
[35] D. C. Marable, S. Shin, A. Y. Nobakht, Investigation into the microscopic mechanisms influencing convective heat transfer of water flow in graphene nanochannels, International Journal of Heat and Mass Transfer 109 (2017) 28–39.
[36] Y.-W. Gu, S. Ge, M. Chen, A molecular dynamics simulation of nanoscale convective heat transfer with the effect of axial heat conduction, Molecular Physics 114 (12) (2016) 1922–1930.
[37] G. Nagayama, P. Cheng, Effects of interface wettability on microscale flow by molecular dynamics simulation, International Journal of Heat and Mass Transfer 47 (3) (2004) 501–513.
[38] A. Haji-Sheikh, J. Beck, D. E. Amos, Axial heat conduction effects in the entrance region of parallel plate ducts, International Journal of Heat and Mass Transfer 51 (25-26) (2008) 5811–5822.
[39] Y. Haddout, J. Lahjomri, The extended graetz problem for a gaseous slip flow in micropipe and parallel-plate microchannel with heating section of finite length: Effects of axial conduction, viscous dissipation and pressure work, International Journal of Heat and Mass Transfer 80 (2015) 673–687.
[40] D. Hennecke, Heat transfer by hagen-poiseuille flow in the thermal development region with axial conduction, Wärme-und Stoffübertragung 1 (3) (1968) 177–184.
[41] H.-E. Jeong, J.-T. Jeong, Extended graetz problem including streamwise conduction and viscous dissipation in microchannel, International Journal of Heat and Mass Transfer 49 (13-14) (2006) 2151–2157.
[42] M. Cieplak, J. Koplik, J. R. Banavar, Boundary conditions at a fluid-solid interface, Physical Review Letters 86 (5) (2001) 803.
[43] J. G. Powles, S. Murad, P. Ravi, A new model for permeable micropores, Chemical physics letters 188 (1-2) (1992) 21–24.
[44] P. A. Thompson, M. O. Robbins, Shear flow near solids: Epitaxial order and flow boundary conditions, Physical review A 41 (12) (1990) 6830.
[45] R. Khare, P. Keblinski, A. Yethiraj, Molecular dynamics simulations of heat and momentum transfer at a solid–fluid interface: relationship between thermal and velocity slip, International journal of heat and mass transfer 49 (19-20) (2006) 3401–3407.
[46] L. Zhang, J. Xu, Q. Chen, S. Wang, Switchable heat transfer in nano janus-interface-system, International Journal of Heat and Mass Transfer 127 (2018) 761–771.
[47] Y. Yu, Y. Tao, Y.-L. He, Molecular dynamics simulation of thermophysical properties of nacl-sio2 based molten salt composite phase change materials, Applied Thermal Engineering 166 (2020) 114628.
[48] B. Bhushan, J. N. Israelachvili, U. Landman, Nanotribology: friction, wear and lubrication at the atomic scale, Nature 374 (6523) (1995) 607–616.
[49] G. J. Wang, N. G. Hadjiconstantinou, Molecular mechanics and structure of the fluid-solid interface in simple fluids, Physical Review Fluids 2 (9) (2017) 094201.
[50] W. J. Huisman, J. F. Peters, M. J. Zwanenburg, S. A. de Vries, T. E. Derry, D. Abernathy, J. F. van der Veen, Layering of a liquid metal in contact with a hard wall, Nature 390 (6658) (1997) 379–381.
[51] D. Chibouti, B. Trouette, E. Chénier, Jump in the conduction heat flux at the gas/solid interface in micro-channels, International Journal of Thermal Sciences 159 106599.
[52] P. A. Thompson, S. M. Troian, A general boundary condition for liquid flow at solid surfaces, Nature 389 (6649) (1997) 360–362.
[53] J. Xu, Y. Li, Boundary conditions at the solid–liquid surface over the multiscale channel size from nanometer to micron, International Journal of Heat and Mass Transfer 50 (13-14) (2007) 2571–2581.
[54] L. Challis, K. Dransfeld, J. Wilks, Heat transfer between solids and liquid helium ii, Proceedings of the Royal Society of London. Series A. Mathematical and Physical Sciences 260 (1300) (1961) 31–46.
[55] D. G. Cahill, W. K. Ford, K. E. Goodson, G. D. Mahan, A. Majumdar, H. J. Maris, R. Merlin, S. R. Phillpot, Nanoscale thermal transport, Journal of applied physics 93 (2) (2003) 793–818.
[56] D. Alexeev, J. Chen, J. H. Walther, K. P. Giapis, P. Angelikopoulos, P. Koumoutsakos, Kapitza resistance between few-layer graphene and water: liquid layering effects, Nano letters 15 (9) (2015) 5744–5749.
[57] N. Shenogina, R. Godawat, P. Keblinski, S. Garde, How wetting and adhesion affect thermal conductance of a range of hydrophobic to hydrophilic aqueous interfaces, Physical Review Letters 102 (15) (2009) 156101.
[58] M. Barisik, A. Beskok, Temperature dependence of thermal resistance at the water/silicon interface, International Journal of Thermal Sciences 77 (2014) 47–54.
[59] G. L. Pollack, Kapitza resistance, Reviews of Modern Physics 41 (1) (1969) 48.
[60] Q. Sun, K.-S. Choi, Y. Zhao, X. Mao, Resistance of velocity slip flow in pipe/channel with a sudden contraction, Physics of Fluids (2020).